Thermoelectric performance in the binary semiconductor compound A_2Se_2 (A = K, Rb) with host-guest structure

Tongcai Yue,[1] Yuming Sun,[1] Yinchang Zhao,[1,*] Sheng Meng,[2,3,†] and Zhenhong Dai[1,‡]
[1]*Department of Physics, Yantai University, Yantai 264005, People's Republic of China*
[2]*Beijing National Laboratory for Condensed Matter Physics and Institute of Physics, Chinese Academy of Sciences, Beijing 100190, People's Republic of China*
[3]*Collaborative Innovation Center of Quantum Matter, Beijing 100084, People's Republic of China*

(Received 29 September 2021; revised 13 December 2021; accepted 20 January 2022; published 7 February 2022; corrected 19 January 2023)

The host-guest structure compounds are potential candidates for high-efficiency thermoelectric (TE) materials because of their good electronic transport combined with ultralow thermal conductivity. In this paper, we theoretically investigate TE transport properties of the hexagonal A_2Se_2 (A = K, Rb) with strongly quartic anharmonicity based on an incorporation of first-principles calculations with self-consistent phonon theory and Boltzmann transport equations. The calculation results reveal that A_2Se_2 (A = K, Rb) have ultralow lattice thermal conductivities κ_L, e.g., 0.30–0.34 W m^{-1} K^{-1} at room temperature, which are only one third of quartz glass. The calculated results indicate that the coexistence of small phonon lifetime τ_{ph} and phonon group velocity υ_{ph} is the reason for the ultralow κ_L in these two host-guest structure materials. Additionally, due to the anisotropic electronic structure, that is, the coexistence of high dispersion and flat band edges, these two materials capture a high TE power factor along the c axis. As a consequence, the anomalous high ZT values of 2.95 and 2.17 at 500 K along the c-axis direction are captured in n-type K_2Se_2 and Rb_2Se_2, which break the long-term record of $ZT < 2$ in most TE materials reported so far. These findings reveal that A_2Se_2 (A = K, Rb) has broad prospects in TE applications.

DOI: 10.1103/PhysRevB.105.054305

I. INTRODUCTION

In recent years, the demand for clean and highly efficient energy has renewed attention to thermoelectric (TE) materials, which can generate electrical energy directly from heat sources without causing additional pollution [1–4]. More importantly, TE devices can use various heat sources (including solar energy, geothermal energy, and waste heat) to achieve clean power generation, which makes TE devices more widely used. Additionally, TE materials can also cool equipment through the Peltier effect [5]. Therefore, it has always been our goal to obtain TE materials with better performance. However, in the TE field, despite a lot of exploration and research, the low conversion efficiency of materials still limits the development of TE applications. Generally, a dimensionless number, called the figure of merit, is used to evaluate the ability of TE materials to generate electrical energy, which is represented by ZT. The TE figure of merit can be defined as $ZT = \frac{S^2\sigma T}{\kappa}$, in which S, σ, T, and κ are the electrical conductivity, thermopower, absolute temperature, and total thermal conductivity (lattice plus electrical thermal conductivity), respectively. In addition, the power factor (PF) is defined as $S^2\sigma$, which characterizes the response of electronic transport performance to temperature gradients in TE materials. Therefore, enhancing ZT refers to adjusting the conflicting material properties by reducing the κ (κ_L plus κ_e) while increasing the power factor $S^2\sigma$. In particular, the most ideal TE material should have the characteristics of phonon-glass electronic crystal (PGEC) [6], which is also the goal we have been pursuing.

So far, most of the promising TE materials studied are small band-gap semiconductors with high electrical conductivity σ, such as cubic Rb_3AuO antiperovskite [7], Ba_2BiAu full-Heusler compound [8], and penta-$PdTe_2$ monolayer [9]. However, the electrical thermal conductivity κ_e is positively correlated with σ and the mutual limitation between them prevents us from using high σ as the only criterion for evaluating good TE materials. Hence, in order to improve the PF in TE material, an anisotropic electronic band structure has been suggested, that is, the dispersion band and flat band edges coexist near the Fermi surface in the same material [10–12]. The former leads to large thermopower, while the latter promotes high electrical conductivity. On the other hand, low lattice thermal conductivity κ_L is also one of the key factors to obtain high TE performance. Generally, it is not difficult to reduce the κ_L, because theoretically κ_L can reach the amorphous solid limit [13–17]. Low κ_L is usually related to strong anharmonicity [18,19], small phonon group velocity υ_{ph} [20,21], and strong phonon scattering [22,23]. Furthermore, some strategies can also reduce κ_L well, such as introducing defects [24–26], reducing size [27,28], and applying strain [29,30]. Apart from TE conversion, low κ_L materials can also be used for thermal

---

[*] Second corresponding author: y.zhao@ytu.edu.cn
[†] smeng@iphy.ac.cn
[‡] First corresponding author: zhdai@ytu.edu.cn

barrier coatings, data storage devices, and thermal management [31–33].

Unfortunately, although these strategies can effectively improve the conversion efficiency of TE materials, the ZT of most reported TE materials is still low. Even at very high temperatures, the ZT value of these TE materials will not exceed 2.5, such as FeNbSb with a $ZT \sim 1.5$ at 1200 K [34], PbTe:Na with a $ZT \sim 1.4$ at 750 K [35], and PbTe-SrTe with a $ZT \sim 2.5$ at 923 K [36]. Recently, due to the ultralow κ_L combined with good electronic properties, a high $ZT > 3$ has been predicted in the a-axis oriented n-type KBaBi with a hexagonal crystal structure [37], breaking the long-term record of $ZT < 2.5$. Nevertheless, the hexagonal KBaBi has not yet been synthesized experimentally, which also provides a new challenge for obtaining good TE materials.

In this paper, inspired by the unique anisotropic structure of the hexagonal crystal system and feasible experimental preparation schemes [38–41], we turn our attention to the α phase A_2Se_2 (A = K, Rb) to obtain available high-ZT materials. Specifically, the anisotropic geometric structure will bring physical insights into the transport properties of materials, and feasible preparation schemes will enable the materials to have greater application potential. Therefore, we theoretically investigate the transport behavior of K_2Se and Rb_2Se_2 by using the self-consistent phonon theory (SCP) combined with the Boltzmann transport equation (BTE). Our main finding is that the alkali-metal atoms can rattle in the pseudocages composed of the Se atoms. The rattling of alkali-metal atoms leads to the the coexistence of strong phonon scattering and softening of acoustic phonon modes. On the other hand, the strong interactions of Se atoms lead to the coexistence of high electronic dispersion band edges and electronic flat band edges, thereby causing good electron transport performance. In addition, the replacement of heavy guest atoms increases the κ_L of the host-guest structure, because the rattling modes of the guest atoms that inhibit κ_L are destroyed [42]. As a result, the anomalous high $ZT > 2.5$ at 500 K along the c axis is captured in the n-type hexagonal K_2Se_2 crystal. Additionally, the n-type Rb_2Se_2 also exhibits excellent TE performance, with ZT exceeding 2 at 500 K along the c axis.

II. METHODOLOGY

.All first-principles calculations are performed in the framework of ground-state Kohn-Sham density functional theory (DFT) [43,44], implemented in the VASP package [45]. In addition, we use the projector-augmented wave method combined with the plane-wave basis set to simulated ions cores and valence electrons. In all DFT calculations, we choose 520 eV as the cutoff energy of the plane-wave basis set, and use the Perdew-Burke-Ernzerhof (PBE) functional [46] to deal with the exchange-correlational interactions. For hexagonal A_2Se_2 (A = K, Rb), the primitive cell contains 12 atoms. In order to obtain the best structure, the hexagonal K_2Se_2 and Rb_2Se_2 are completely relaxed in a $7 \times 7 \times 10$ k-point sampling, until the energy convergence and the norms of all the forces are less than 10^{-6} eV and 5×10^{-3} eV/Å, respectively. Furthermore, according to the density functional perturbation theory (DFPT) [47], we also calculated the Bonn effective charges and dielectric tensors needed for the nonanalytic part in the dynamic matrix. For investigating the bonding properties, we calculated the electron localization function of A_2Se_2 (A = K, Rb) with $7 \times 7 \times 10$ k-point meshes.

For calculating the phonon and thermal transport properties, the interatomic force constants (IFCs) (second to sixth order) are captured from the ALAMODE code [48,49]. First, we captured the second-order IFCs by virtue of the finite-displacement approach in a $1 \times 1 \times 2$ supercell with displacement of 0.01 Å [50]. Then, we performed the 3000-step *ab initio* molecular dynamics (AIMD) simulations with the time step of 2 fs to obtain 60 snapshots at 300 K, and then the 60 snapshot atoms move in random directions 0.1 Å, and get 60 quasirandom structures. Next, the third- and sixth-order IFCs are trained by using the compressive sensing lattice dynamics (CSLD) method [51] in the 60 quasirandom structures. Based on the calculated IFCs combined with the phonon Boltzmann transport equation, we obtained the harmonic and anharmonic phonon and thermal transport properties of K_2Se_2 and Rb_2Se_2. Based on the relaxation time approximation (RTA), the κ_L tensor is written as

$$\kappa_L^{\alpha\beta}(T) = \frac{1}{N_q\Omega}\sum_{q,j} C_{q,j}(T)\upsilon_{q,j}^{\alpha}\upsilon_{q,j}^{\beta}\tau_{q,j}(T), \tag{1}$$

where Ω is the unit cell volume, N_q is the number of wave vectors, α and β denote Cartesian coordinates directions, q and j are the signs of phonon modes, $C_{q,j}$ is the specific heat capacity, $\upsilon_{q,j}^{\alpha(\beta)}$ is the phonon group velocity, and $\tau_{q,j}(T)$ is the phonon lifetime. Additionally, Matthiessen's rule is used to estimate the phonon lifetime, which is written as

$$\tau_{q,j}^{-1}(T) = 2\big[\Gamma_{q,j}^{\text{anh}}(T) + \Gamma_{q,j}^{\text{iso}}(T)\big], \tag{2}$$

in which $\Gamma_{q,j}^{\text{anh}}(T)$ are three-phonon scattering rates and $\Gamma_{q,j}^{\text{iso}}(T)$ are phonon isotope scattering rates. For SCP calculations, the anharmonic renormalization of phonon frequencies is captured from effective (second- and fourth-order) IFCs. Finally, κ_L^{HA} and κ_L^{SCP} are obtained in $12 \times 12 \times 14$ k-point samplings by using the BTE of the RTA.

We also calculated the electronic transport in these two materials using the AMSET package [52] based on the electron BTE. The code uses the fully anisotropic acoustic deformation potential (ADP) method to treat the electron-acoustic phonon interaction, including the perturbations from longitudinal (transversal) modes and anisotropy in the deformation response to support the anisotropic materials. On the other hand, the electro-optical phonon interaction is treated by using the polar optical phonon (POP) method. Moreover, the effect of ionized impurity scattering is also included. We use the PBE functional to calculate the electronic band structure, high-frequency dielectric constants, and deformation potentials. The DFPT with the PBE functional was used to capture the static dielectric constants, effective polar phonon frequency, and elastic constants. The HSE06 functional is used to capture the rational band gap. On this basis, we recalculate the electronic structure in a dense $47 \times 47 \times 59$ k-point grid in order to capture the rational electron relaxation time τ_e and electronic transport properties. By using Fermi's "golden rule," the different scattering rate of materials from initial state

TABLE I. The calculated lattice constants (a^{opt} and a^{opt}) (in Å) and irreducible elastic constants (in GPa) for K_2Se_2 and Rb_2Se_2, where we have five independent components. The experimental lattice constants (a^{opt}) quoted from Ref. [39] are listed for comparison.

Semiconductor	a^{opt}	a^{expt}	c^{opt}	c^{expt}	C_{11}	C_{12}	C_{13}	C_{33}	C_{44}	C_{66}
K_2Se_2	9.03	8.91	6.09	6.04	29.1	13.0	8.4	21.4	8.3	8.1
Rb_2Se_2	9.42	9.21	6.34	6.20	24.7	11.8	8.3	15.5	7.5	6.5

$\psi_{n\mathbf{k}}$ to final state $\psi_{m\mathbf{k+q}}$ can be written as

$$\tilde{\tau}^{-1}_{n\mathbf{k}\to m\mathbf{k+q}} = \frac{2\pi}{\hbar}|g_{nm}(\mathbf{k},\mathbf{q})|^2\delta(\varepsilon_{n\mathbf{k}}-\varepsilon_{m\mathbf{k+q}}), \tag{3}$$

in which n and m are the signs of the energy level, $\mathbf{k}$ and $\mathbf{k}+\mathbf{q}$ denote the coordinates of reciprocal space, $\varepsilon_{n\mathbf{k}}$ is the energy state $\psi_{n\mathbf{k}}$, and $g_{nm}(\mathbf{k},\mathbf{q})$ is the electron-phonon scattering matrix element from initial state $\psi_{n\mathbf{k}}$ into final state $\psi_{m\mathbf{k+q}}$. Finally, the rational carrier relaxation time, τ, can be calculated as

$$\frac{1}{\tau^{\mathrm{tot}}} = P^{\mathrm{ADP}} + P^{\mathrm{POP}} + P^{\mathrm{IMP}}, \tag{4}$$

where P^{ADP}, P^{POP}, and P^{IMP} are the scattering rate of the completely anisotropic acoustic deformation potential, the scattering rate of the polar optical phonon, and the scattering rate of the ionized impurity, respectively. For details, please refer to the Supplemental Material [53]. In addition, these two materials' parameters from first-principles calculations, including dielectric tensors, phonon frequencies, and elastic constants, are listed in Table S1 in the Supplemental Material [53].

III. RESULTS AND DISCUSSION

The α-phase A_2Se_2 (A = K, Rb) crystallize in the Na_2O_2-type hexagonal lattice structure with the $P\bar{6}2m$[189] space group. The atomic structure of these two materials is noncentrosymmetric, and the unit cell contains six alkali-metal (A = K, Rb) atoms and six Se atoms. Using the PBE exchange-correlational functional, the optimized lattice constants for hexagonal K_2Se_2 and Rb_2Se_2 are listed in Table I, and the experimental lattice constants [39] are also listed for comparison. The results indicate that the calculated values are consistent with the observed experimental values. Generally, the geometric structure is a key factor affecting the transport performance of TE materials. For the hexagonal A_2Se_2 (A = K, Rb), the Se atoms comprise a pseudocage, and alkali-metal atoms fill the pseudocages, forming the host-guest structure. Analogously to clathrates, the hexagonal A_2Se_2 (A = K, Rb) is expected to bring physical insights to the investigation of the transport properties.

Furthermore, we investigate mechanical and thermodynamic stability for K_2Se_2 and Rb_2Se_2. The calculated elastic constants of these two materials are listed in Table I. For the hexagonal crystal structure, the mechanical stability criteria are written as

$$C_{11} > |C_{12}|, \quad C_{33}(C_{11}+C_{12}) > 2C_{13}^2, \quad C_{44} > 0. \tag{5}$$

The calculated results indicate that the elastic constants of these two materials satisfy the above stability criteria [54], and K_2Se_2 and Rb_2Se_2 are mechanically stable. In addition, the thermodynamic stability of these two materials is checked, and the composition phase diagrams A_xSe_{1-x} (A = K, Rb) are shown in Figs. S1(a) and S1(b) in the Supplemental Material [53]. The results indicate that A_xSe_{1-x} (A = K, Rb) are thermodynamically stable [55,56]. Moreover, the stabilities of K_2Se_2 and Rb_2Se_2 at high temperature are estimated by using AIMD simulations with 40 ps (20 000 steps). The results indicate that K_2Se_2 and Rb_2Se_2 are stable at 500 K.

For the vibrational properties, we investigate the harmonic phonon dispersion curves of K_2Se_2 and Rb_2Se_2, as shown by the light cyan lines in Figs. 1(c) and 1(d). For these two materials, there are no imaginary frequencies in the phonon dispersion curves, which means that they are dynamically stable. In addition, considering the nonanalytic correction of the phonon spectrum caused by the dipole-dipole interaction, the optical phonon branch is divided into two branches at Γ; one is the transverse optical phonon branch, and the other is the longitudinal optical phonon branch. Due to the heavier Rb atoms, the phonon frequency of Rb_2Se_2 is lower than that of K_2Se_2, which usually means that the phonon group velocity υ_{ph} of Rb_2Se_2 is smaller. Meantime, the low phonon group velocity υ_{ph} in Rb_2Se_2 also results in a small κ_L [see Eq. (1)].

On this basis, we also consider the effect of the renormalization of phonon energies caused by the quartic anharmonicity to thermal transport in K_2Se_2 and Rb_2Se_2. Based on the CSLD method combined with SCP theory, the temperature dependent anharmonic phonon dispersion curves are plotted in Figs. 1(c) and 1(d). With the increase of temperature, we clearly observe that the low-lying phonon modes below 80 cm^{-1} have obvious hardening in K_2Se_2 due to strong anharmonicity of Se atoms. In Rb_2Se_2, the hardening of low-lying phonon modes is due to the common contribution of Rb and Se atoms, because the Rb atom is also the main component of low-frequency phonon branches. In addition, the intermediate frequency optical phonon branch mainly contributed by the vibration of the K atoms is also significantly hardened, manifesting that the K atoms also have a strong anharmonicity. In contrast, most intermediate frequency optical phonon branches corresponding to the vibrations of Rb and Se atoms are only slightly hardened. This unique vibration property related to K atoms is similar to the action of "rattling" modes in cage compounds, showing a strong temperature dependence in K_2Se_2. These rattling modes can be confirmed by the weak bonding strength of the K atoms, because there are few local electrons around the K atoms, as shown in Fig. 6. Additionally, the anharmonic renormalization of the phonon frequencies in these two materials reduces the high-frequency optical phonon branches composed of the relative vibration of Se atoms. To sum up, the κ_L of these two materials will increase after considering the quartic anharmonicity, because it is mainly contributed by the acoustic and low-frequency optical phonon branches.

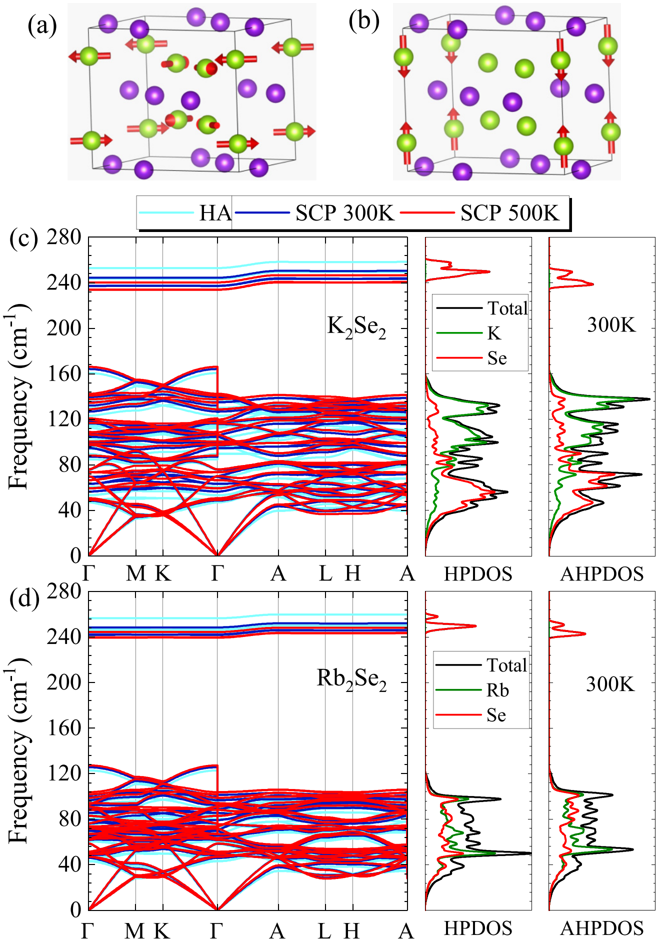

FIG. 1. The vibration modes of the Se atoms in (a) the 22 phonon branches and (b) the 36 phonon branches at the Γ point for α-M_2Se_2 (A = K, Rb) ($P\bar{6}2m$), where purple and green balls represent the A (A = K, Rb) atoms and Se atoms, respectively. The above vibration modes are visualized using VESTA software [57]. (c, d) The harmonic phonon dispersion curves and phonon density of states (HPDOS), anharmonic phonon dispersion curves, and phonon density of states (AHPDOS) for (c) K_2Se_2 and (d) Rb_2Se_2. For phonon dispersion curves, the violet and red lines signify the anharmonic dispersion curves at 300 and 500 K, respectively, while the light cyan lines signify the harmonic dispersion curves. For HPDOS and AHPDOS, the black, olive, and red lines signify the total and partial PDOS of alkali-metal atoms and selenium atoms, respectively. For the AHPDOS, we only show the result at 300 K.

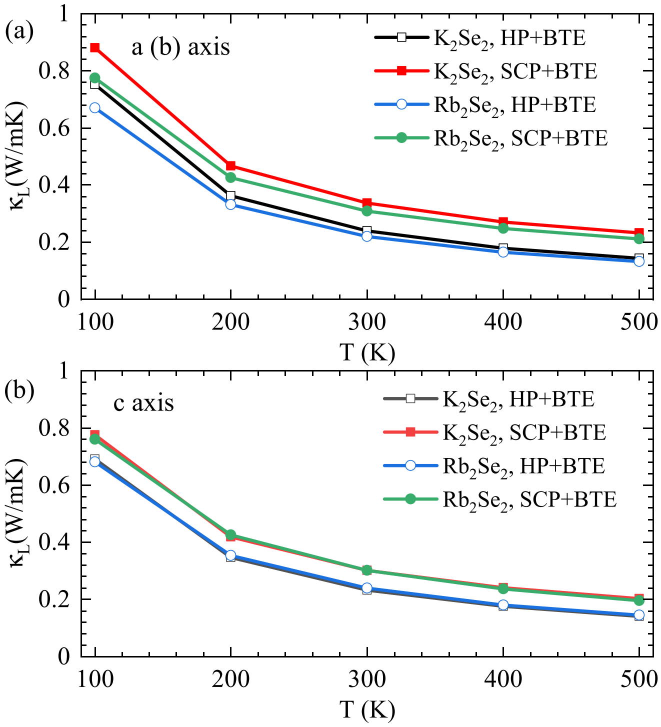

FIG. 2. The temperature-dependence lattice thermal conductivities κ_L(T) of K_2Se_2 and Rb_2Se_2 by using the SCP theory combined with the phonon BTE along the (a) a or b axis and (b) c axis, respectively. In addition, the combination of HP and phonon BTE results of these two materials is also exhibited for comparison.

In order to further investigate the relationship between the vibration properties and the crystal structure, we also calculate the PDOS of unequal atoms and the visual vibration modes at the Γ point for these two materials, as shown in Fig. 1 and in Fig. S2 in the Supplemental Material [53]. At first, it is worth noting that K_2Se_2 and Rb_2Se_2 have the same high-frequency optical phonon branches near 240 cm^{-1}, which mainly consist of Se atoms. Furthermore, we found that the two peaks of the high-frequency optical phonon branches are mainly composed of unequal relative vibrations of Se atoms. Generally, the high-frequency phonon branches consist of lighter atoms' vibrations, while low-frequency phonon branches consist of heavier atoms. This anomalous phenomenon is unique and interesting because the Se atom is not a light element in these two materials. In order to explore the underlying physical mechanism of this unique phenomenon, we research the vibration modes of the Se atoms in the highest and second highest optical phonon modes at the Γ point [see Figs. S2(e) and S2(f) in the Supplemental Material [53]]. Since the alkali-metal atoms' contribution to the high-frequency optical phonon branches is small, we only investigate the vibration of the Se atoms. The results exhibited that the highest and second highest optical phonon modes at the Γ point are mainly caused by relative vibration of the unequal Se atom pairs along the z direction.

We also investigated the bonding properties of these two materials from the two-dimensional projected electron localization function [58], as shown in Figs. 6(a) and 6(b). In the (100) plane, there are more local electrons between Se atom pairs along the z direction, which means that there is a relatively strong bond between them. Meanwhile, the strong bond between Se atom pairs makes the relative vibration between them more intense, causing the vibration of the heavier atoms to dominate the high-frequency phonon branches. While the rattling mode of K atoms suppresses the collective vibration of the crystal, it softens the acoustic phonon modes, thereby reducing the phonon group velocity υ_{ph}. Additionally, since the the electrons near Se atoms are more localized in the (001) plane, the bond around the Se atom is weaker. Therefore, the relative vibration of the Se atoms along the xy plane direction contributes to the low-frequency optical phonon branches. The result is consistent with the corresponding atomic

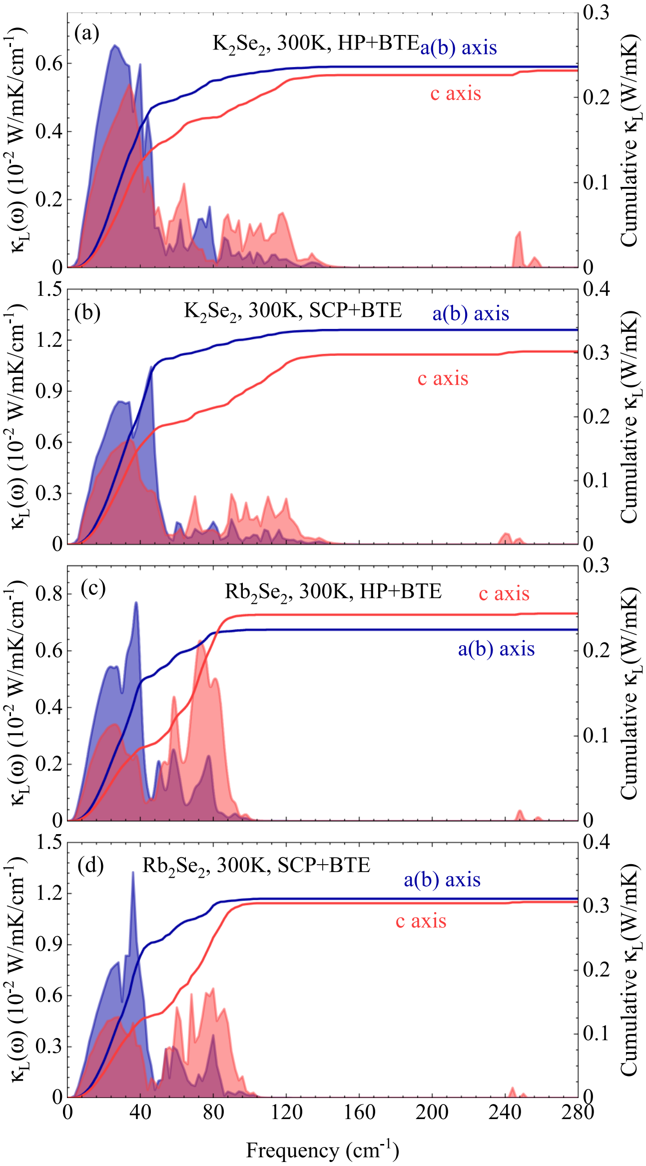

FIG. 3. Lattice thermal conductivity spectra $\kappa_L(\omega)$ (filled area below the curves) and relevant cumulative κ_L in K_2Se_2 and Rb_2Se_2 (lines). Royal and red colors signify the *a*- and *b*-axis directions and *c*-axis direction, respectively. (a) $\kappa_L^{\mathrm{HA}}(\omega)$ and relevant cumulative κ_L^{HA} for K_2Se_2. (b) $\kappa_L^{\mathrm{SCP}}(\omega)$ and relevant cumulative κ_L^{SCP} for K_2Se_2 at 300 K. (c) $\kappa_L^{\mathrm{HA}}(\omega)$ and relevant cumulative κ_L^{HA} for Rb_2Se_2. (d) $\kappa_L^{\mathrm{SCP}}(\omega)$ and relevant cumulative κ_L^{SCP} for Rb_2Se_2 at 300 K.

vibration [Fig. 1(a)]. In summary, the alkali-metal atoms rattling in the Se anion framework lead to the softening of acoustic phonon modes, thereby reducing the acoustic phonon group velocity (υ_{ph}). This is a benefit to lower thermal conductivity.

Now, we turn to investigate the lattice thermal conductivity κ_L, which plays an important role in the fields of thermoelectricity and thermal management. The calculated harmonic and anharmonic κ_L of these two materials are shown in Fig. 2, which shows the anisotropic thermal transport behavior along *a* and *c* axes, respectively. We predicted the harmonic lattice thermal conductivity κ_L^{HA} of 0.23 (0.24) and 0.24 (0.22) W K^{-1} m^{-1} along the *c* (*a* and *b*) axis at 300 K in K_2Se_2 and Rb_2Se_2, respectively, which are only a quarter of the κ of quartz glass ($\approx$0.9 W K^{-1} m^{-1}). Moreover, we also calculate the anharmonic lattice thermal conductivity κ_L^{SCP} by taking into account the influence of anharmonic renormalization of the phonon energies. The values of κ_L^{SCP} are 0.34 (0.30) and 0.31 (0.30) W K^{-1} m^{-1} along the *c* (*a* and *b*) axis at 300 K in K_2Se_2 and Rb_2Se_2, respectively, which are obviously higher than κ_L^{HA}. The calculated results exhibited that the anharmonic renormalization of phonon energies plays an important role in thermal transport. Remarkably, even considering the hardening of phonon frequencies by anharmonic renormalization, the κ_L^{SCP} of these two materials is still ultralow, which is only one third of quartz glass. For the *a*-axis (*b*-axis) direction, the κ_L of Rb_2Se_2 is significantly lower than that of K_2Se_2, which can be explained as the heavier Rb atom resulting in a smaller υ_{ph}. Anomalously, Rb_2Se_2, despite the heavier Rb atom, exhibits a higher κ_L than K_2Se_2 along the *c* axis. We find that the heavier Rb atom suppressed the rattling mode of the guest atom, resulting in the decrease in phonon scattering, that is, the increase in phonon lifetime. This interesting phenomenon is consistent with $ZnSe_2$ ($\kappa_L \sim 0.69$ W K^{-1} m^{-1}) [59] and $CdSe_2$ ($\kappa_L \sim 0.75$ W K^{-1} m^{-1}) [60]. The results indicate that the the replacement of the heavier guest atom inhibits the rattling modes, thereby decreasing the phonon scattering.

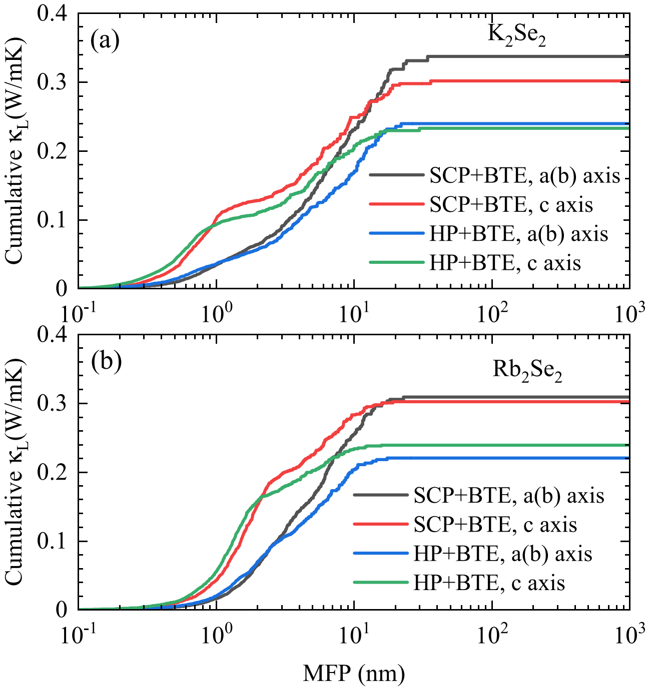

FIG. 4. The cumulative κ_L as a function of the maximum of phonon mean free paths (MPMFPs) at 300 K for (a) α-K_2Se_2 and (b) α-Rb_2Se_2.

Furthermore, we can approximately use a power function $\kappa_L \sim T^{-\alpha}$ to describe the temperature dependence of the lattice thermal conductivity. For the harmonic lattice thermal conductivity κ_L^{HA}, the α values are 1.04 (0.99) and 1.01 (0.96) along the *c* (*a* and *b*) axis in K_2Se_2 and Rb_2Se_2, respectively, while the anharmonic lattice thermal conductivity κ_L^{SCP} has a weak temperature dependence due to the anharmonic

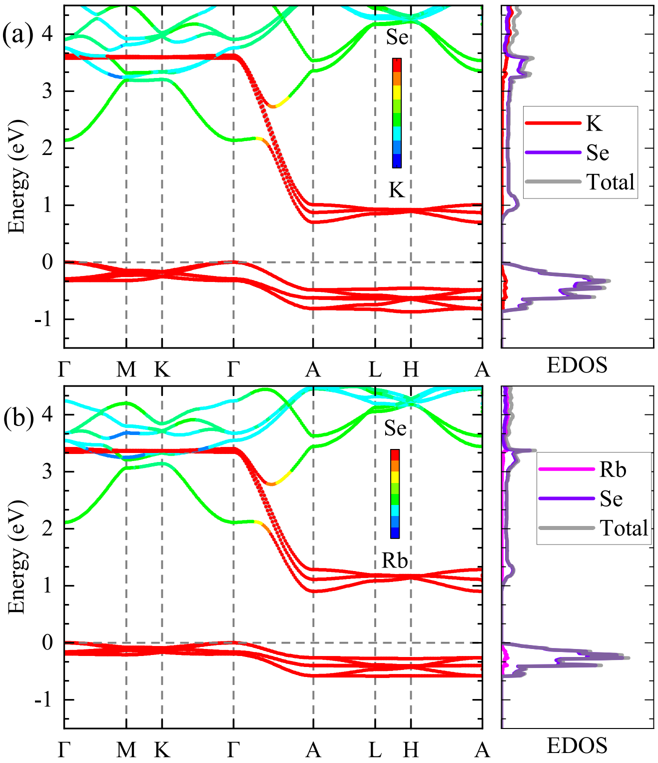

FIG. 5. The calculated projected electronic band structure and corresponding electronic density of states (EDOS) for (a) K_2Se_2 and (b) Rb_2Se_2 using the PBE functional. In particular, the Fermi energy level is set at 0 eV.

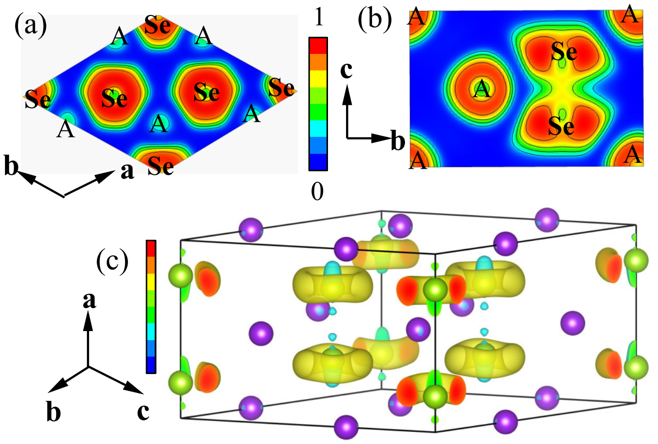

FIG. 6. The two-dimensional (2D) projection electron local function (ELF) in the (a) (001) plane and (b) (010) plane for A_2Se_2 (A = K, Rb). The ELF value range from 0 to 1, in which 1 represents the fully localized electrons and 0 represents completely delocalized electrons. The distances from the origin are 1.82 and 5.21 Å in the (001) plane and (100) plane, respectively. (c) The charge density difference for A_2Se_2 (A = K, Rb). Blue signifies that the atom loses electrons, and red signifies that the atom gains electrons. The above 2DELF are visualized using VESTA software [57].

renormalization of phonon energies, and the α values are 0.86 (0.85) and 0.83 (0.84) along the c (a and b) axis in K_2Se_2 and Rb_2Se_2, respectively. Obviously, the κ_L along the c-axis direction exhibits a weaker temperature dependence than that along the a-axis direction, which is due to the strong anharmonicity caused by the combination of the rattling mode and the strong bonding of the Se atom pair.

In order to clarify the microscopic mechanism of ultralow κ_L and the influence of anharmonic renormalization of the phonon frequencies on κ_L for these two materials, we analyze many factors that affect κ_L, for instance, phonon frequencies ω, phonon group velocity υ_{ph}, and phonon lifetime τ_{ph}. First, we researched the lattice thermal conductivity spectra $\kappa_L(\omega)$ and corresponding cumulative κ_L for K_2Se_2, as shown in Fig. 3. In our calculations, the $\kappa_L^{\mathrm{SCP}}(\omega)$ exhibits a shape similar to $\kappa_L^{\mathrm{HA}}(\omega)$, and has a tendency to move to higher phonon energy due to the hardening of the low-lying phonon branches, which is consistent with the trend of the phonon spectrum. In addition, the peak values of $\kappa_L(\omega)$ have been significantly improved after considering anharmonic renormalization of the phonon frequencies. Additionally, $\kappa_L(\omega)$ show that acoustic phonon branches mainly contribute to κ_L for K_2Se_2. In contrast, a large part of κ_L for Rb_2Se_2 is composed of low-frequency optical phonon branches. This is because the low-frequency optical phonon branches shift down and close to acoustic phonon branches, so that the optical phonon modes also participate in the thermal conduct. Furthermore, these downward-moving optical phonon branches enhance phonon-phonon scattering, thereby reducing the lattice thermal conductivity.

Except for the influence of phonon frequencies ω_{ph}, the phonon group velocity υ_{ph} also plays a crucial role in κ_L because $\upsilon_{\mathrm{ph}}^2 \propto \kappa_L$ [see Eq. (1)]. Obviously, due to the hardening of the low-frequency phonon mode caused by anharmonic renormalization, the phonon group velocity υ_{ph} of these two materials increases, as shown in Fig. S3 in the Supplemental Material [53]. In addition, the acoustic phonon branches of these two materials have a higher υ_{ph} due to the larger phonon dispersion. Additionally, there is a large υ_{ph} along the c axis in low-frequency optical phonon branches because of the vibration of Se atoms. Due to the hybridization of alkali-metal atoms and Se atoms, the low-frequency optical phonon branches have soft dispersion along the a-axis and b-axis direction, which makes them have a smaller υ_{ph}. Additionally, the last important factor is the phonon lifetime τ_{ph}, which is proportional to κ_L [see Eq. (1)]. In our calculations, we consider the three-phonon scattering processes and the isotope scattering processes for these two materials, while the former is usually more important. The three-phonon scattering rate is determined by the three-phonon scattering phase space (W) and the Grüneisen parameter (γ). The former represents the number of three-phonon scattering channels, and the latter represents the anharmonic interaction between atoms. The calculated τ_{ph}, γ, and W are shown in Fig. S4 in the Supplemental Material [53]. As expected, the low-frequency optical phonon branch also has a relatively long phonon lifetime τ_{ph}, which further supports our previous analysis of $\kappa_L(\omega)$ along the c axis. Additionally, τ_{ph} for Rb_2Se_2 is obviously longer than that for K_2Se_2 in low-frequency optical phonon branches, which is the cause of higher κ_L along the c axis in Rb_2Se_2. In addition, the anharmonic renormalization of phonon

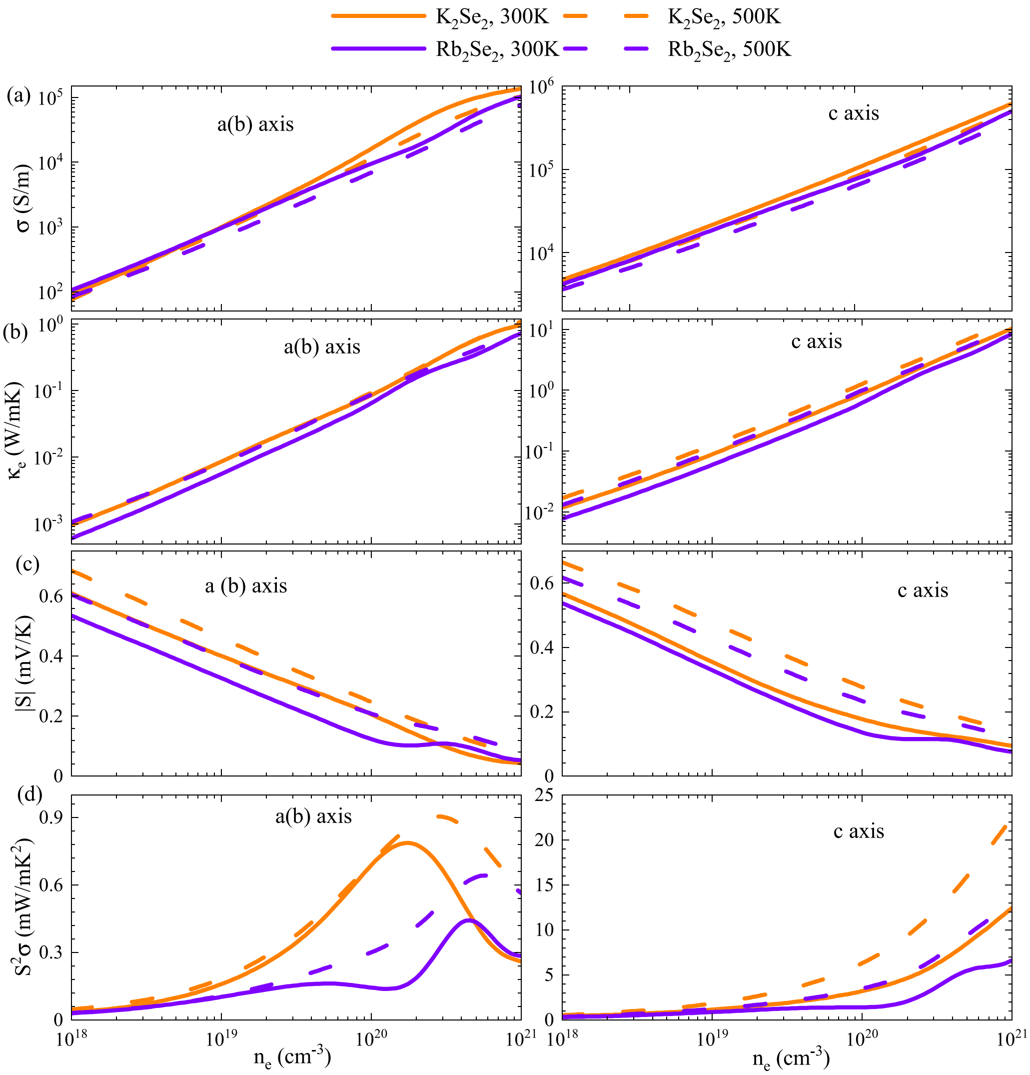

FIG. 7. The electronic transport parameters for *n*-type K_2Se_2 and *n*-type Rb_2Se_2. (a) Electrical conductivity σ along the $a(b)$ axis (left) and along the c axis (right). (b) Electrical thermal conductivity κ_e along the $a(b)$ axis (left) and along the c axis (right). (c) Seebeck coefficient S along the $a(b)$ axis (left) and along the c axis (right). (d) Power factor $S^2\sigma$ along the $a(b)$ axis (left) and along the c axis (right).

frequencies increases τ_{ph}, which is reflected in the increased γ and W for these two materials, as shown in Fig. S4 in the Supplemental Material [53]. As the result, the combination of small τ_{ph} and small υ_{ph} explains the origin of the ultralow κ_L of these two materials.

Additionally, nanostructuring can capture lower κ_L, because the reduction in size limits the phonon mean free paths (MFPs). Figure 4 shows the cumulative κ_L as the maximum phonon MFPs at 300 K for these two materials. In our calculations, the maximum values of κ_L^{HA} (κ_L^{SCP}) corresponding to maximum phonon MFPs are 21.93 (34.18), 29.79 (35.89), 17.41 (22.81), and 15.76 (19.18) nm for K_2Se_2 along a and b axes, K_2Se_2 along the c axis, Rb_2Se_2 along a and b axes, and Rb_2Se_2 along the c axis, respectively. If the maximum phonon MFP is limited to 10 nm, all κ_L^{SCP} will be less than 0.28 $\mathrm{W\,K^{-1}\,m^{-1}}$, and the minimum value can even reach 0.20 $\mathrm{W\,K^{-1}\,m^{-1}}$ for K_2Se_2 along the c axis. For κ_L considering the anharmonic renormalization of phonon energies, we did not consider the influence of four-phonon scattering and grain boundary scattering, so κ_L was overestimated [22].

If these two materials have good electronic transport performance, they will have broad prospects in thermoelectric application. Based on the PBE exchange-correction functional, the band gaps of K_2Se_2 and Rb_2Se_2 are 0.701 and 0.902 eV, respectively. Since the PBE exchange-correction functional always underestimates the band gap of semiconductors, we also calculate the band gap of the HSE06 exchange-correction functional. The PBE electronic band structures for these two materials are plotted in Fig. 5, and the HSE06 electronic band structures are plotted in Fig. S5 in the Supplemental Material [53]. K_2Se_2 and Rb_2Se_2 have similar electronic band structures and belong to the indirect band-gap semiconductors. In addition, the conduction band minimum (CBM) is situated at the A point and the valence band maximum (VBM) is located at the Γ point. The band gaps of the HSE06 exchange-correction functional are 1.663 and 1.869 eV for K_2Se_2 and Rb_2Se_2, respectively. Since the electronic band structures calculated by using HSE06 and PBE functionals are not significantly different except for the band gap, we use the electronic band structure and corresponding electronic density of states (EDOS) of PBE calculations to qualitatively investigate the electronic transport properties of these two materials. Apparently, the pseudocage composed of Se atoms is the main contributor to the electronic band structure near the Fermi level, which is consistent with other similar structures [59,60]. In addition, the pseudocage leads to an anisotropic electronic band structure along the z direction near the CBM edge, that is, the coexistence of high dispersion and flat band edge. The anisotropic band edge leads to high electrical conductivity and large Seebeck coefficient. The results further confirm our previous conclusion, that is, the host-guest structure reduces κ_L while maintaining good electronic transport performance.

Moreover, we also calculate the charge density difference for A_2Se_2 (A = K, Rb) in order to investigate the charge transfer between the atoms of these two materials, as shown in Fig. 6(c). Since the electrons around the K atom are almost fully localized, its contribution to the electronic band structure is small. Therefore, we pay more attention to the contribution of Se atom pairs to the electron band structure. We find that the Se atom pairs along the z direction lose electrons, while the Se atom pairs along the xy plane gain electrons. The results are very consistent with the distribution of the Se atomic orbital EDOS (see Fig. S6 in the Supplemental Material [53]), that is, the $p_{x/y}$ orbital of the Se atom mainly contributes to the VBM, while the p_z orbital mainly contributes to the CBM. Obviously, the large EDOS near the VBM proves that there are more electrons in the Se atom along the xy plane direction, which will result in a larger S in p-type K_2Se_2 and Rb_2Se_2. Additionally, the p_z orbital of the Se atom has a large EDOS near the CBM, which means that n-type K_2Se_2 and Rb_2Se_2 have larger S along the c-axis direction.

The electronic band structure indicates that these two materials with electron doping are expected to have good electronic transport properties along the c-axis direction. In order to confirm the above analysis, we calculate the carrier scattering rates (see Fig. S7 in the Supplemental Material [53]) and corresponding transport behavior for these two materials (see Fig. 7 and see Fig. S8 in the Supplemental Material [53]) by considering the ADP, POP, and ionized impurity scattering. To capture a rational electronic transport behavior, the band gap of the HSE06 functional is used as the input parameter for these two materials. The calculated results show excellent TE performance for n-type K_2Se_2 and Rb_2Se_2. Due to the anisotropic electronic band structure along the c axis, the existence of large S and σ results in a high power factor in these two materials with n-type doping. Due to the large dispersion band along the Γ-A point at the CBM, an anomalously high electrical conductivity σ is obtained. As the temperature increases, the scattering rates increases, resulting in a significant decrease in σ. In addition, κ_e and σ exhibit the same trend, which can be explained by the Wiedemann-Franz law ($\kappa_e = L\sigma T$). L signifies the Lorenz number, which is usually constant. Furthermore, the flat band results in large S because of the high EDOS near the CBM. Finally, the maximum PF will exceed 20 $\mathrm{mW/(mK^2)}$ in K_2Se_2 along the c axis at 500 K. Additionally, the p-type A_2Se_2 (A = K, Rb) have also good electronic transport properties due to large S.

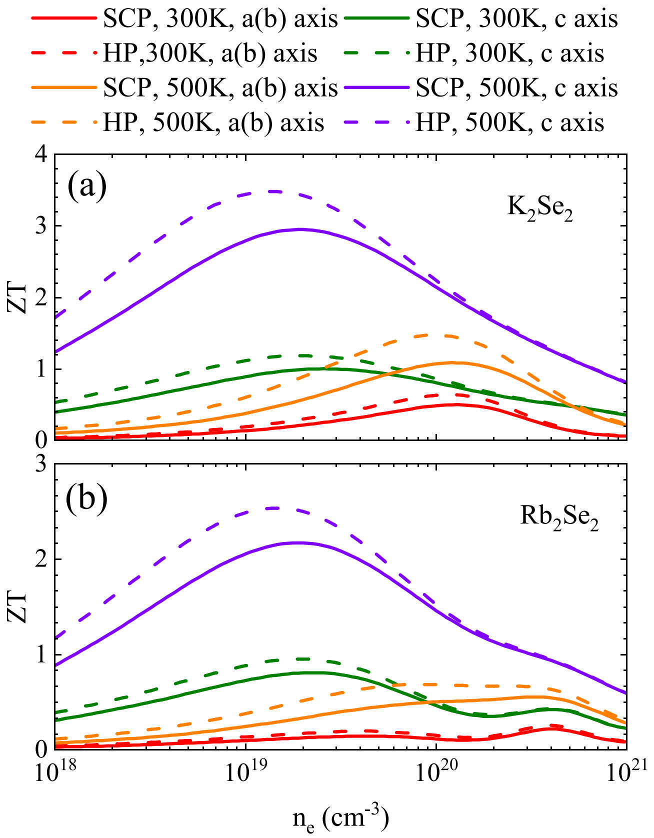

FIG. 8. The dimensionless TE figure of merit for (a) n-type K_2Se_2 and (b) n-type Rb_2Se_2.

Combined with the ultralow κ_L, the phonon-glass electronic-crystal characteristics is captured in these two materials. The calculated TE figure of merit with temperature and carrier concentration for these two materials is shown in Fig. 8 and in Fig. S9 in the Supplemental Material [53]. Based on the SCP (harmonic phonon theory) lattice thermal conductivity, the optimal ZT is 2.95 (3.44) for K_2Se_2 at $n_e = 2 \times 10^{19}$ (1×10^{19}) $\mathrm{cm^{-3}}$ at 500 K along the c axis due to the coexistence of high PF and ultralow κ_L as shown in Fig. S10 in the Supplemental Material [53]. Additionally, the n-type K_2Se_2 has also high ZT; the value is 1.0 along the c axis at 300 K using the SCP results. Additionally, the n-type Rb_2Se_2 also exhibits a high $ZT \sim 2.17$ at $n_e = 2 \times 10^{19}$ $\mathrm{cm^{-3}}$ at 500 K along the c axis using the SCP theory. Due to the large EDOS near the VBM, the p-type Rb_2Se_2 captured maximum $ZT \sim 1.73$ at $n_h = 5 \times 10^{20}$ $\mathrm{cm^{-3}}$ at 500 K along the c axis using the SCP theory. The value of ZT calculated by κ_L of the HP+BTE method gives the upper limit, while ZT calculated by the SCP+BTE method gives the lower limit. Even considering the lower limit of ZT, the results indicate that n-type K_2Se_2 and Rb_2Se_2 still have excellent TE performance. In addition, low electron doping concentration and a feasible preparation scheme mean that these two materials are more competitive in the application of thermoelectric materials.

IV. CONCLUSION

In summary, we use first-principles calculations combined with SCP theory and the Boltzmann transport equation to systematically investigate the thermal transport and TE transport properties of K_2Se_2 and Rb_2Se_2. Due to the unique anisotropic guest-host structure, the phonon-glass electron-crystal features are captured along the *c*-axis direction in *n*-type K_2Se_2 and Rb_2Se_2. The calculations show that the alkali-metal atom rattles in the cages composed of Se atoms, causing the coexistence of strong phonon scattering and small phonon group velocity, thereby reducing κ_L. In addition, the lighter guest atom leads to stronger rattling modes in the host-guest structure, resulting in increased phonon scattering. Meanwhile, the cage composed of Se atoms leads to the coexistence of high dispersion and flat band edge near the CBM. Due to the anisotropic electronic band structure leading to the coexistence of high σ and large S, these two materials also exhibit good electronic properties; e.g., at the optimal doping concentration, *n*-type K_2Se_2 exceeds 2.5 at 500 K along the *c*-axis direction. Therefore, the anomalous *ZT* of 2.95 is captured along the *c* axis in *n*-type K_2Se_2. Meantime, the optimal *ZT* of 2.17 is obtained along the *c* axis in *n*-type Rb_2Se_2. This paper emphasizes the use of anisotropic bonding of the host-guest structure to capture ultralow κ_L, and reveals the crucial role of guest atoms in phonon scattering processes. In addition, we clarify the correction of κ_L and the corresponding microscope mechanism through the anharmonic renormalization of phonon energies.

ACKNOWLEDGMENTS

This research was supported by the National Natural Science Foundation of China under Grants No. 11974302, No. 11774396, and No. 12174327 and by Shandong Natural Science Funds for Doctoral Program under Grant No. ZR2019BA009.

[1] D. Dangić, E. D. Murray, S. Fahy, and I. Savić, Phys. Rev. B **101**, 184110 (2020).

[2] R. D'Souza, J. Cao, J. D. Querales-Flores, S. Fahy, and I. Savić, Phys. Rev. B **102**, 115204 (2020).

[3] C. Kumarasinghe and N. Neophytou, Phys. Rev. B **99**, 195202 (2019).

[4] W. Wang, Z. Dai, Q. Zhong, Y. Zhao, and S. Meng, Chin. Phys. B **29**, 126501 (2020).

[5] K. Uchida, R. Iguchi, S. Daimon, R. Ramos, A. Anadón, I. Lucas, P. A. Algarabel, L. Morellón, M. H. Aguirre, M. R. Ibarra, and E. Saitoh, Phys. Rev. B **95**, 184437 (2017).

[6] L. M. Daniels, S. N. Savvin, M. J. Pitcher, M. S. Dyer, J. B. Claridge, S. Ling, B. Slater, F. Corà, J. Alaria, and M. J. Rosseinsky, Energy Environ. Sci. **10**, 1917 (2017).

[7] Y. Zhao, C. Lian, S. Zeng, Z. Dai, S. Meng, and J. Ni, Phys. Rev. B **102**, 094314 (2020).

[8] J. Park, Y. Xia, and V. Ozoliņš, Phys. Rev. Appl. **11**, 014058 (2019).

[9] Y.-S. Lan, X.-R. Chen, C.-E. Hu, Y. Cheng, and Q.-F. Chen, J. Mater. Chem. A **7**, 11134 (2019).

[10] L. D. Hicks and M. S. Dresselhaus, Phys. Rev. B **47**, 12727 (1993).

[11] D. Parker, X. Chen, and D. J. Singh, Phys. Rev. Lett. **110**, 146601 (2013).

[12] D. I. Bilc, G. Hautier, D. Waroquiers, G.-M. Rignanese, and P. Ghosez, Phys. Rev. Lett. **114**, 136601 (2015).

[13] D. G. Cahill, S. K. Watson, and R. O. Pohl, Phys. Rev. B **46**, 6131 (1992).

[14] D. T. Morelli, V. Jovovic, and J. P. Heremans, Phys. Rev. Lett. **101**, 035901 (2008).

[15] G. P. Meisner, D. T. Morelli, S. Hu, J. Yang, and C. Uher, Phys. Rev. Lett. **80**, 3551 (1998).

[16] G. S. Nolas, J. L. Cohn, G. A. Slack, and S. B. Schujman, Appl. Phys. Lett. **73**, 178 (1998).

[17] M. D. Nielsen, V. Ozolins, and J. P. Heremans, Energy Environ. Sci. **6**, 570 (2013).

[18] Y. Zhao, C. Lian, S. Zeng, Z. Dai, S. Meng, and J. Ni, Phys. Rev. B **101**, 184303 (2020).

[19] Q. Zhong, Z. Dai, W. Wang, Y. Zhao, and S. Meng, Int. J. Energy Res. **45**, 6958 (2021).

[20] A. Hori, S. Minami, M. Saito, and F. Ishii, Appl. Phys. Lett. **116**, 242408 (2020).

[21] W. Wang, Z. Dai, X. Wang, Q. Zhong, Y. Zhao, and S. Meng, Int. J. Energy Res. **45**, 20949 (2021).

[22] Y. Xia, K. Pal, J. He, V. Ozoliņš, and C. Wolverton, Phys. Rev. Lett. **124**, 065901 (2020).

[23] Y. Zhao, Z. Dai, C. Zhang, C. Lian, S. Zeng, G. Li, S. Meng, and J. Ni, Phys. Rev. B **95**, 014307 (2017).

[24] K.-Q. Chen, W.-X. Li, W. Duan, Z. Shuai, and B.-L. Gu, Phys. Rev. B **72**, 045422 (2005).

[25] G. Yang, R. Niu, L. Sang, X. Liao, D. R. G. Mitchell, N. Ye, J. Pei, J.-F. Li, and X. Wang, Adv. Energy Mater. **10**, 2000757 (2020).

[26] B. Jiang, Y. Yu, J. Cui, X. Liu, L. Xie, J. Liao, Q. Zhang, Y. Huang, S. Ning, B. Jia, B. Zhu, S. Bai, L. Chen, S. J. Pennycook, and J. He, Science **371**, 830 (2021).

[27] Q. Zhong, Z. Dai, J. Liu, Y. Zhao, and S. Meng, Phys. E **115**, 113683 (2020).

[28] L. H. Liang and B. Li, Phys. Rev. B **73**, 153303 (2006).

[29] N. F. Hinsche, B. Y. Yavorsky, I. Mertig, and P. Zahn, Phys. Rev. B **84**, 165214 (2011).

[30] B. Geisler and R. Pentcheva, Phys. Rev. Mater. **2**, 055403 (2018).

[31] B. Koley, A. Lakshan, P. R. Raghuvanshi, C. Singh, A. Bhattacharya, and P. P. Jana, Angew. Chem., Int. Ed. **60**, 9106 (2021).

[32] R. Yang, G. Chen, and M. S. Dresselhaus, Nano Lett. **5**, 1111 (2005).

[33] J. Sootsman, D. Chung, and M. Kanatzidis, Angew. Chem., Int. Ed. **48**, 8616 (2009).

[34] C. Fu, S. Bai, Y. Liu, Y. Tang, L. Chen, X. Zhao, and T. Zhu, Nat. Commun. **6**, 8144 (2015).

[35] Y. Pei, A. LaLonde, S. Iwanaga, and G. J. Snyder, Energy Environ. Sci. **4**, 2085 (2011).

[36] G. Tan, F. Shi, S. Hao, L.-D. Zhao, H. Chi, X. Zhang, C. Uher, C. Wolverton, V. P. Dravid, and M. G. Kanatzidis, Nat. Commun. **7**, 12167 (2016).

[37] Z. Feng, Y. Fu, Y. Yan, Y. Zhang, and D. J. Singh, Phys. Rev. B **103**, 224101 (2021).

[38] P. Böttcher, J. Getzschmann, and R. Keller, Z. Anorg. Allg. Chem. **619**, 476 (1993).

[39] A. Jain, S. P. Ong, G. Hautier, W. Chen, W. D. Richards, S. Dacek, S. Cholia, D. Gunter, D. Skinner, G. Ceder, and K. A. Persson, APL Mater. **1**, 011002 (2013).

[40] D. P. Thompson and P. Boudjouk, J. Org. Chem. **53**, 2109 (1988).

[41] R. Niewa, Significance of ammonothermal synthesis for nitride materials, in *Ammonothermal Synthesis and Crystal Growth of Nitrides: Chemistry and Technology*, edited by E. Meissner and R. Niewa (Springer, New York, 2021), pp. 3–12.

[42] D. Voneshen, K. Refson, E. Borissenko, M. Krisch, A. Bosak, A. Piovano, E. Cemal, M. Enderle, M. Gutmann, M. Hoesch *et al.*, Nat. Mater. **12**, 1028 (2013).

[43] P. Hohenberg and W. Kohn, Phys. Rev. **136**, B864 (1964).

[44] W. Kohn and L. J. Sham, Phys. Rev. **140**, A1133 (1965).

[45] G. Kresse and J. Furthmüller, Phys. Rev. B **54**, 11169 (1996).

[46] J. P. Perdew, K. Burke, and M. Ernzerhof, Phys. Rev. Lett. **77**, 3865 (1996).

[47] S. Baroni, S. de Gironcoli, A. Dal Corso, and P. Giannozzi, Rev. Mod. Phys. **73**, 515 (2001).

[48] T. Tadano and S. Tsuneyuki, Phys. Rev. B **92**, 054301 (2015).

[49] T. Tadano, Y. Gohda, and S. Tsuneyuki, J. Phys.: Condens. Matter **26**, 225402 (2014).

[50] K. Esfarjani and H. T. Stokes, Phys. Rev. B **77**, 144112 (2008).

[51] F. Zhou, B. Sadigh, D. Åberg, Y. Xia, and V. Ozoliņš, Phys. Rev. B **100**, 184309 (2019).

[52] A. M. Ganose, J. Park, A. Faghaninia, R. Woods-Robinson, K. A. Persson, and A. Jain, Nat. Commun. **12**, 1 (2021).

[53] See Supplemental Material at http://link.aps.org/supplemental/10.1103/PhysRevB.105.054305 for the calculating method of different scattering rates, as well as the figures of the free energy, the convex hull, the harmonic phonon density of states, the anharmonic phonon density of states, the atomic vibration modes, the group velocity of phonons, phonon lifetimes, the Grüneisen parameter, three-phonon scattering phase space, electronic band structures using HSE06, the electron scattering rate, electronic transport parameters, electrical conductivity, electrical thermal conductivity, the Seebeck coefficient, power factors, and the dimensionless TE figure of merit for $A_2\text{Se}_2 (A = \text{K, Rb})$.

[54] Z.-j. Wu, E.-j. Zhao, H.-p. Xiang, X.-f. Hao, X.-j. Liu, and J. Meng, Phys. Rev. B **76**, 054115 (2007).

[55] J. E. Saal, S. Kirklin, M. Aykol, B. Meredig, and C. Wolverton, Jom **65**, 1501 (2013).

[56] S. Kirklin, J. E. Saal, B. Meredig, A. Thompson, J. W. Doak, M. Aykol, S. Rühl, and C. Wolverton, npj Comput. Mater. **1**, 1 (2015).

[57] K. Momma and F. Izumi, J. Appl. Crystallogr. **41**, 653 (2008).

[58] A. Savin, R. Nesper, S. Wengert, and T. F. Fassler, Angew. Chem., Int. Ed. Engl. **36**, 1808 (1997).

[59] T. Jia, J. Carrete, Z. Feng, S. Guo, Y. Zhang, and G. K. H. Madsen, Phys. Rev. B **102**, 125204 (2020).

[60] T. Jia, J. Carrete, Y. Zhang, and G. K. H. Madsen, Low thermal conductivities and excellent thermoelectric performances of the pyrite-type IIB-VIA2 dichalcogenides: ZnS2, CdS2 and CdSe2, arXiv:2005.05916 (2020).

Correction: Labels for the first and second corresponding authors were missing and have been inserted.